Selective treatment and monitoring of disseminated cancer micrometastases in vivo using dual-function, activatable immunoconjugates

Bryan Q. Spring[a,1], Adnan O. Abu-Yousif[a,1], Akilan Palanisami[a,2], Imran Rizvi[a,2], Xiang Zheng[a], Zhiming Mai[a], Sriram Anbil[a], R. Bryan Sears[a,3], Lawrence B. Mensah[a], Ruth Goldschmidt[a], S. Sibel Erdem[a], Esther Oliva[b], and Tayyaba Hasan[a,c,d,4]

[a]Wellman Center for Photomedicine, Massachusetts General Hospital and Harvard Medical School, Boston, MA 02114; Departments of [b]Pathology and [c]Dermatology, Massachusetts General Hospital, Boston, MA 02114; and [d]Division of Health Sciences and Technology, Harvard University and Massachusetts Institute of Technology, Cambridge, MA 02139

Drug-resistant micrometastases that escape standard therapies often go undetected until the emergence of lethal recurrent disease. Here, we show that it is possible to treat microscopic tumors selectively using an activatable immunoconjugate. The immunoconjugate is composed of self-quenching, near-infrared chromophores loaded onto a cancer cell-targeting antibody. Chromophore phototoxicity and fluorescence are activated by lysosomal proteolysis, and light, after cancer cell internalization, enabling tumor-confined photocytotoxicity and resolution of individual micrometastases. This unique approach not only introduces a therapeutic strategy to help destroy residual drug-resistant cells but also provides a sensitive imaging method to monitor micrometastatic disease in common sites of recurrence. Using fluorescence microendoscopy to monitor immunoconjugate activation and micrometastatic disease, we demonstrate these concepts of "tumor-targeted, activatable photoimmunotherapy" in a mouse model of peritoneal carcinomatosis. By introducing targeted activation to enhance tumor selectivity in complex anatomical sites, this study offers prospects for catching early recurrent micrometastases and for treating occult disease.

activatable therapeutic agent | activatable imaging agent | photodynamic therapy | ovarian cancer | molecular imaging

Metastatic disease remains the main cause of cancer-related death despite advances in cytoreductive surgery and chemotherapy (1–4). An ongoing dilemma is the lack of options to address residual micrometastases that escape standard treatments and detection by current imaging technologies (3). In addition to spread via hematogenous and lymphatic routes (5), diffuse micrometastatic spread throughout anatomical cavities is also problematic, including peritoneal dissemination resulting from cancers of the colon (6), pancreas (7), and ovary (1, 2, 4). These obstacles are pronounced in the treatment of epithelial ovarian cancer (EOC), a prime example of a frequently recurrent disease characterized by residual micrometastases. Due to the lack of screening methods or distinct symptoms during early progression, the vast majority of EOC cases are diagnosed once the disease has metastasized and formed numerous nodules studding the peritoneal cavity (1, 2, 4). Although a significant fraction of patients (~35%) appear to achieve a complete response after cytoreductive surgery and follow-up chemotherapy, a small number of cells with intrinsic or acquired resistance are responsible for recurrence and poor survival (1, 2, 4, 8). These residual micrometastases are clinically occult until gross recurrence, which is often refractory to standard treatments (1, 2, 4). Laparotomy, an invasive surgical reassessment, frequently fails to detect residual disease (9) while noninvasive clinical imaging modalities also have poor sensitivity for subcentimeter tumors (10, 11).

To address the challenges associated with treating and detecting occult, residual, and drug-resistant micrometastases before gross

recurrence, it is necessary to develop (*i*) targeted treatments with high tumor selectivity and distinct mechanisms of cell death (12–14) to overcome dose-limiting toxicities and chemoresistance; and (*ii*) high-resolution approaches with sufficient contrast to monitor microscopic disease. Here, we address both of these needs by developing an activatable construct targeted to markers overexpressed by cancer cells with dual functionality for both therapy and imaging, and integrate this into a quantitative fluorescence microendoscopy platform for longitudinal monitoring of micrometastases. This approach realizes treatment selectivity and imaging fidelity at the microscale.

Targeted agents carrying "always-on," unquenched chromophores have emerged for targeted therapy and imaging at the macroscale. In a promising clinical study, intraoperative visualization of EOC nodules labeled with a targeted, always-on fluorescent probe facilitated the identification of more tumor deposits by surgeons compared with conventional bright-field illumination (15). This development may ultimately translate to fluorescence-guided resection for more radical cytoreductive surgery, leaving less disease behind (15–17). Photoimmunotherapy (PIT) using always-on immunoconjugates is a targeted form of photodynamic therapy—first reported in the seminal works of

Significance

Residual micrometastases following standard therapies limit our ability to cure many cancers. This article demonstrates a new therapy and visualization platform that targets residual cancer micrometastases with enhanced sensitivity and selectivity based on "tumor-targeted activation." This targeted activation feature not only provides a potent therapeutic arm that is effective against chemoresistant disease while minimizing side effects due to nonspecific toxicities but also enables micrometastasis imaging in common sites of disease recurrence to screen patients harboring residual tumor deposits. This approach offers promise for treating and monitoring drug-resistant micrometastases presently "invisible" to clinicians.

Levy and colleagues (18)—that has been shown to hold promise by us (19–23) and by others (18, 24, 25). Because photodynamic agents are mechanistically distinct from traditional treatment modalities (13, 14), are effective against radioresistant and chemoresistant cells (19, 20, 26), and can also resensitize resistant cells to chemotherapy (20, 23), the development of PIT is of importance for overcoming drug resistance. In fact, photodynamic therapy has been used in the treatment of disseminated peritoneal disease with some success intraoperatively (27) and endoscopically in the lung, bladder, and esophagus (*SI Text*, Note S1).

Integrating the concepts of targeted therapy and imaging, a recent proof-of-concept study performed dual epidermal growth factor receptor (EGFR)-targeted PIT and imaging of localized, macroscopic tumors using always-on immunoconjugates (25). This study used a mouse model derived from s.c. implantation of A431 squamous-cell carcinoma cells that express abnormally high levels of EGFR (25). A limitation of PIT is persistent phototoxicity and background signal in nontarget tissues due to unbound and circulating always-on immunoconjugates, which compromise treatment and imaging selectivity at the microscale. It therefore remains uncertain whether PIT is safe and effective for treatment of micrometastases—the ultimate test of treatment selectivity. It is also unknown whether always-on immunoconjugates have sufficient tumor selectivity for treatment and imaging of tumors that express more realistic levels of the target molecule. Given these limitations, we sought to develop a more selective type of PIT—termed tumor-targeted, activatable PIT (taPIT)—and tumor imaging based on dual-function immunoconjugates that enable activatable, near-infrared (NIR)-mediated PIT as well as activatable fluorescence imaging (Fig. 1). This approach—building on the concept of lysosome-activated imaging probes suggested by Achilefu, Urano, Kobayashi, and coworkers (28, 29)—not only achieves greater treatment selectivity than always-on PIT but also enables resolution of microscopic tumor deposits.

Here, we demonstrate these concepts of dual-function, tumor-targeted activatable immunoconjugates for selective treatment and quantitative, longitudinal imaging of micrometastases in vivo using a clinically motivated model of advanced-stage ovarian carcinomatosis (30). In this model, peritoneal micrometastases are derived from human EOC cells (OVCAR5) that possess intrinsic resistance to chemotherapy (8, 31). Using activatable immunoconjugates, a custom-built microendoscope (32) and a newly developed image analysis workflow (Figs. S2 and S3), we present minimally invasive, quantitative, and repeated measurements of micrometastases during therapy. Using fluorescence microendoscopy to characterize immunoconjugate pharmacokinetics and to monitor micrometastatic burden reduction in vivo, we demonstrate tumor-selective immunoconjugate activation and taPIT efficacy. This targeted activation significantly reduces nonspecific phototoxicity and fluorescence to provide therapeutic response monitoring of microscopic tumor nodules in a complex model of disseminated disease.

Results

Quantitative Fluorescence Microendoscopy-Guided taPIT Platform. We developed an integrated therapeutic and imaging platform using quantitative fluorescence microendoscopy with dual-function, activatable immunoconjugates to treat and visualize micrometastatic nodules in vivo (Fig. 1). First, we quantified tumor-targeted activation of the immunoconjugate in vivo (Fig. 2) as well as micrometastasis imaging accuracy (Fig. 3). To optimize treatment selectivity and dosimetry, we applied longitudinal fluorescence microendoscopy to characterize immunoconjugate pharmacokinetics and tumor selectivity dynamics in vivo (Fig. 4). Next, we demonstrated that tumor-targeted activation reduces nontarget phototoxicity compared with a number of control agents—including unconjugated, always-on agents—while realizing selective destruction of micrometastases in vivo (Fig. 5).

Finally, we confirmed micrometastasis imaging accuracy by histopathologic grading of specimens ex vivo coregistered with in vivo fluorescence microendoscope images (Fig. 6).

The immunoconjugate used in this study is comprised of Food and Drug Administration-approved photodynamic and anti-EGFR therapeutic agents (Fig. 1*A*; *SI Text*, Notes S2 and S3) previously demonstrated to reduce metastatic EOC burden synergistically when used in combination as unconjugated, individual agents (12). Cetuximab, an anti-EGFR monoclonal antibody (mAb), targets cancer cells overexpressing EGFR. EGFR is an important molecule for targeting cancer cells that displays elevated expression in up to 70% of EOCs (33) and in many other carcinomas (34) (*SI Text*, Note S4). Although EGFR targeting is the focus here, immunoconjugate synthesis, imaging, and taPIT are all generalizable such that a variety of targeting molecules for other tumor antigens may be applied (*SI Text*, Note S2). Benzoporphyrin derivative (BPD) is a clinically approved NIR photoactivatable and cytotoxic chromophore that undergoes electronic excited singlet state quenching upon antibody conjugation—as described by Savellano and Hasan (35)—with increasing self-quenching in parallel with higher loading ratios (*SI Text*, Note S5). This quenching phenomenon increases the tumor specificity when optimally designed; however, excess BPD loading results in the loss of cancer cell-specific delivery. In a series of chemical synthesis and in vitro cell culture studies, we previously identified an optimal conjugation ratio of approximately seven BPD molecules per mAb molecule, Cet-BPD(1:7), as a strongly quenched (sevenfold) and cancer cell-specific construct (35) that retains the biological activity of cetuximab (36). These in vitro studies suggest that, like cetuximab, Cet-BPD is trafficked to lysosomes as part of the EGFR internalization and degradation pathway where more than one-half of the Cet-BPD immunoconjugates release BPD resulting in dequenching and activation of both BPD phototoxicity and fluorescence emission in cell culture (37). Note that the immunoconjugate has a minimal, but nonnegligible, baseline level of phototoxicity and fluorescence emission in the quenched state.

Although these prior in vitro studies offered promise, we sought to test the true measures of taPIT and activatable tumor imaging—enhancement of micrometastasis treatment selectivity and imaging accuracy in vivo. We hypothesized that Cet-BPD could serve as both a molecular-targeted, activatable therapeutic agent and imaging probe for selectively treating and monitoring microscopic tumor deposits in vivo. Here, we show that—in vivo—Cet-BPD is selectively activated within micrometastases and imparts selective tumor cytotoxicity upon NIR irradiation.

In vivo Cet-BPD imaging was achieved using a custom-built microendoscope (32) to detect occult micronodules in a mouse model of EOC characterized by disseminated metastases (30) (Fig. 1*E*). The microendoscope probe enters the peritoneal cavity via a 14-gauge catheter traversing the abdominal wall (Fig. 1*D*) without the need for surgery or sutures. In vivo fluorescence microendoscopy before (day 0, no-tumor control) and at various days following tumor inoculation (days 5 and 14, tumor) show the specificity of Cet-BPD fluorescence for micrometastases (Fig. 1*E*). To verify the presence and absence of tumor in these mice, we applied an anti-human cytokeratin 8 (CK8) immunostain specific for human EOC cells and also stained microvasculature (anti-mouse platelet endothelial cell adhesion molecule, or CD31), which is initially absent but becomes tortuous after neoangiogenesis within advanced EOC nodules (Fig. 1*E* and Figs. S3 and S4).

Tumor-Selective Immunoconjugate Activation. To demonstrate tumor-specific activation of Cet-BPD in vivo, we used quantitative imaging methods validated by conventional techniques. taPIT toxicity, Cet-BPD imaging, and Cet-BPD tissue extraction studies were conducted using constructs with varying degrees of BPD quenching (Fig. 2*A*). Cet-BPD fluorescence was investigated at various scales, from macroscopic biodistribution to microscopic
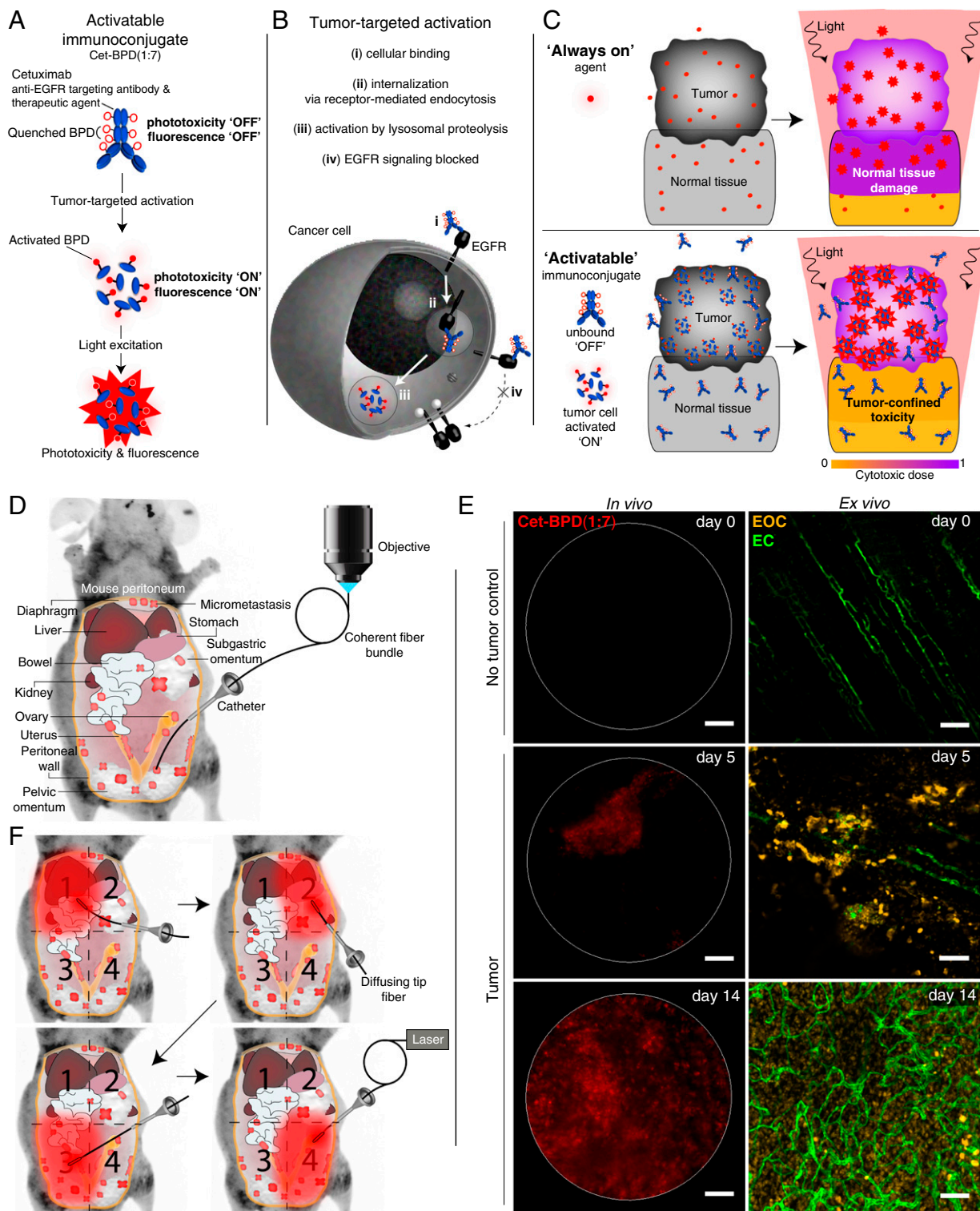
www.manaraa.com

Fig. 1. Concepts of tumor-targeted, activatable photoimmunotherapy (taPIT) and longitudinal monitoring of micrometastases in vivo. (*A*) Cet-BPD—a dual-function, activatable immunoconjugate for both taPIT and monitoring of micrometastases—consists of multiple BPD molecules conjugated to each cetuximab molecule. The BPD molecules remain self-quenched until EGFR binding and cellular internalization. (*B*) Schematic of Cet-BPD intracellular activation. (*C*) taPIT enables tumor-confined phototoxicity, whereas always-on agents and immunoconjugates result in nonspecific damage to normal tissues. (*D*) Mouse model of micrometastatic epithelial ovarian cancer (EOC) and fluorescence microendoscopy schematics. (*E*) (*Left*) In vivo fluorescence microendoscopy of control no-tumor and EOC mice on days 5 and 14 posttumor inoculation. (*Right*) Corresponding ex vivo immunofluorescence images show human EOC and mouse endothelial cells (ECs) stained with anti-CK8 and -CD31 antibodies, respectively. (Scale bars: 100 μm.) Note that all images in this report are displayed on a linear scale deliberately without saturation. Nonlinear, saturated image display appears to show higher contrast, but such a representation is not quantitative (Fig. S1). (*F*) Schematic of i.p. Cet-BPD photoactivation using a diffusing tip fiber and scattering media to enable efficient, targeted wide-field treatment of micrometastatic disease spread throughout the abdominal cavity by stepwise irradiation of each quadrant within the cavity.
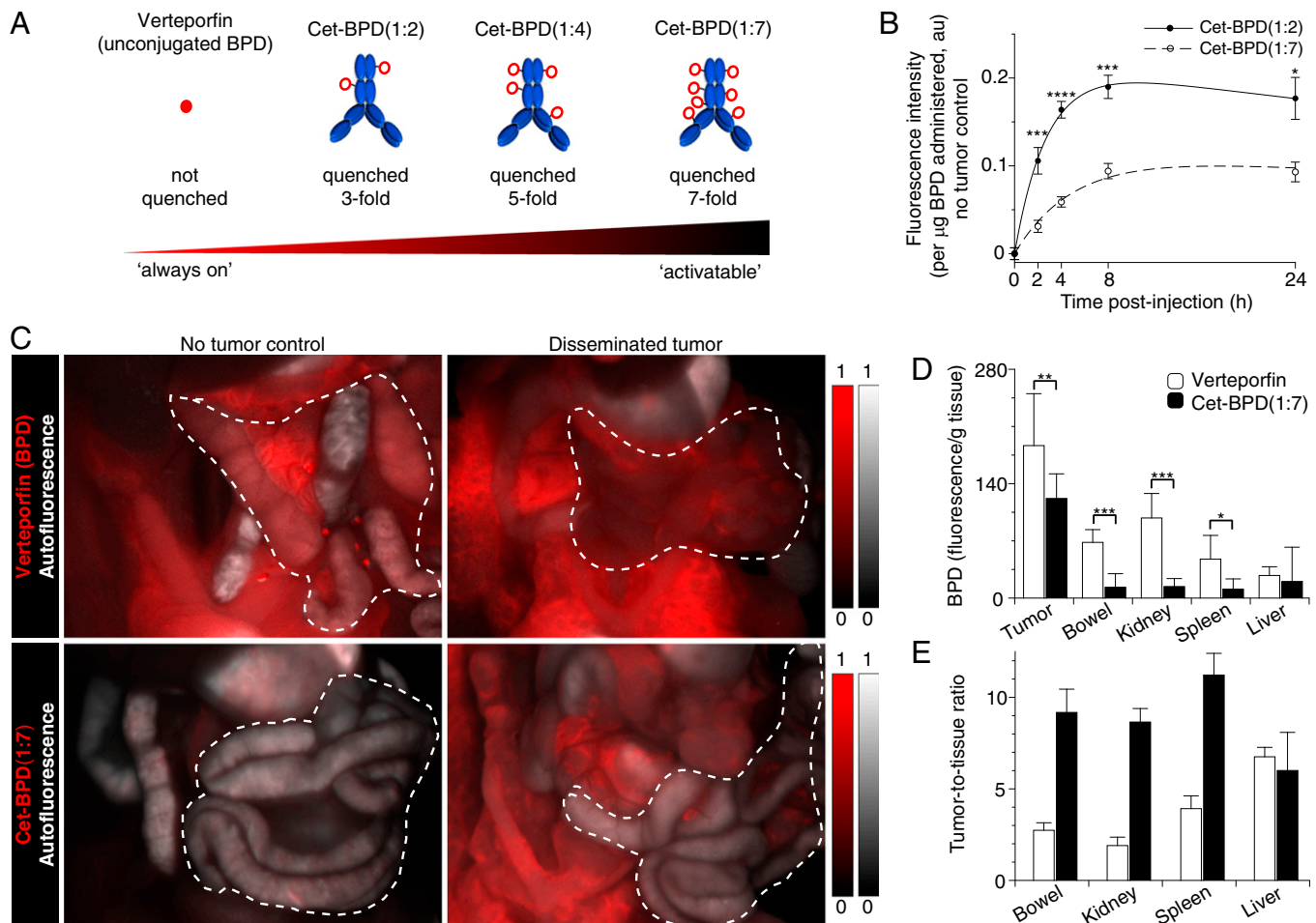
Spring et al.

Fig. 2. In vivo Cet-BPD activation in tumors versus nontarget tissues. (*A*) Constructs with varying BPD quenching efficiencies. (*B*) In vivo fluorescence microendoscopy of Cet-BPD(1:7) (1.4 mg of cetuximab; *n* = 4 mice, 160 fields) shows reduced nonspecific fluorescence compared with Cet-BPD(1:2) (1.4 mg of cetuximab; *n* = 3 mice, 120 fields) in control, no-tumor mice (mean ± SEM; *P < 0.05, ***P < 0.001, ****P < 0.0001, two-tailed unpaired *t* test). (*C*) Spectrally unmixed BPD fluorescence (red) and autofluorescence (gray scale) from hyperspectral fluorescence images of the bowel (outlined in each image; see also images of the entire peritoneal cavity, Fig. S5) 2 h after verteporfin or 48 h after Cet-BPD(1:7) administration. Intensity scales are matched for no-tumor control and EOC mice (day 23). (*D*) Quantification of BPD in peritoneal tissues of EOC mice (day 10) by extraction. (*E*) Tumor-to-tissue ratios for Cet-BPD(1:7) (*n* = 15 mice; binned data from 8, 12, and 24 h postadministration to reduce noise) versus verteporfin (*n* = 10 mice; binned data from 2 and 4 h post-administration) calculated from *D* (mean ± SEM; *P < 0.05, **P < 0.01, ***P < 0.001, ****P < 0.0001, two-tailed unpaired *t* test).

intratumoral localization. These results confirmed that Cet-BPD (1:7) largely remains quenched in normal tissue in vivo. Cet-BPD (1:7) displayed approximately twofold less nonspecific fluorescence than Cet-BPD(1:2) per BPD molecule administered (Fig. 2*B*), in agreement with the 2.3-fold increased quenching strength of Cet-BPD(1:7) previously characterized in vitro (35).

We next investigated activation of Cet-BPD in multifocal tumors studding vital peritoneal organs. In situ imaging-based biodistribution studies at fixed time points revealed enhanced tumor specificity of activatable Cet-BPD(1:7) compared with verteporfin, the present clinical, liposomal formulation of always-on BPD. Hyperspectral fluorescence imaging of the peritoneal cavity—at the macroscopic scale—was validated by Cet-BPD extraction studies from pulverized tissues at matched time points. These data indicate low tumor selectivity for verteporfin (Fig. 2 *C–E*); e.g., verteporfin has a tumor-to-bowel ratio of 2.7 (Fig. 2*D*). In contrast, Cet-BPD(1:7) has a much lower signal in the bowel and other sensitive organ tissues than verteporfin, achieving a tumor-to-bowel ratio of 9.2 (Fig. 2 *C–E*). However, this is a conservative estimate as the Cet-BPD signal in nontumor tissue is at the lower detection limit. Fitting the pharmacokinetic data to a model (*SI Text*) suppresses noise and indicates tumor-

to-bowel ratios of 2.8 for verteporfin and 18.6 for Cet-BPD. This improved tumor selectivity is also seen in the hyperspectral fluorescence images following spectral deconvolution. The bowel is outlined in each image to highlight decreased BPD signal for Cet-BPD(1:7) compared with verteporfin (Fig. 2*C* and Fig. S5). Thus, activatable immunoconjugates for taPIT significantly reduce bowel toxicity (Fig. S6*A*)—the major obstacle in the clinical translation of photodynamic therapy of intraperitoneal (i.p.) metastases (38).

To quantify the 3D microscale localization of activated Cet-BPD immunoconjugates within micrometastases, we performed confocal microscopy on freshly excised tissues. Immunostains for human EOC cells, mouse endothelial cells (ECs), and mouse immune cells were applied ex vivo. We were able to detect clusters of EOC cells with BPD fluorescence in tissues excised from tumor-bearing mice, but not in healthy mice (Fig. 3*A*). To assess the tumor specificity of Cet-BPD activation quantitatively, we designed a pixel-by-pixel tumor classification test based on a Cet-BPD fluorescence intensity threshold from which we determined Cet-BPD sensitivity (fraction EOC pixels correctly identified) and specificity (1 – fraction EOC pixels incorrectly identified) (Fig. 3*B*). The optimal threshold, determined by receiver operating characteristic
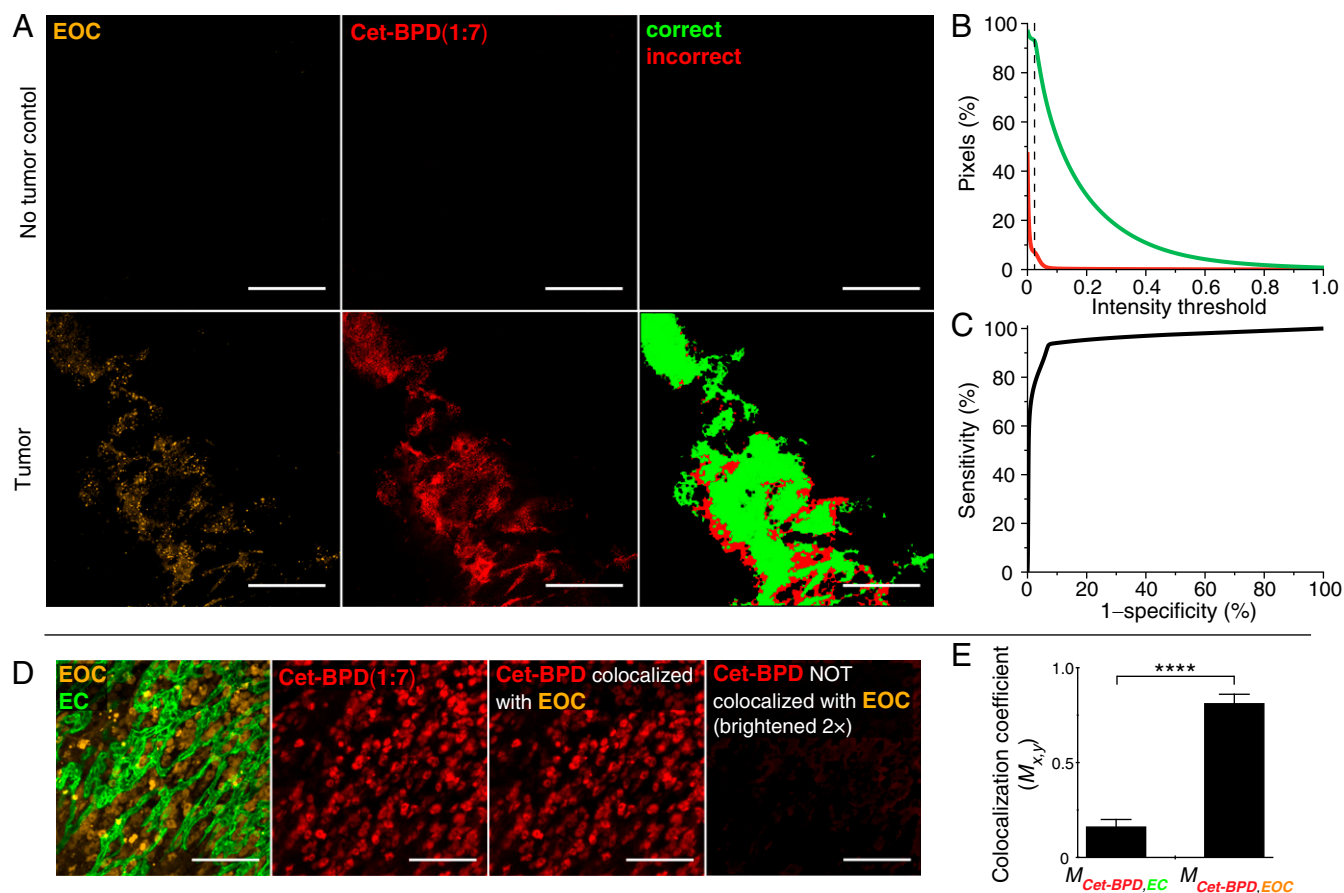
Fig. 3. Microscale localization of activated Cet-BPD in vivo. (*A*) Cet-BPD fluorescence confocal image mosaics of freshly excised tissue from control no-tumor and EOC mice. The locations of human EOC cells (anti-human CK8 stain) are also shown for comparison, as well as pixels correctly and incorrectly classified as tumor based on the optimal Cet-BPD intensity threshold shown in *B*. (*B*) The green and red curves represent the percentage of pixels correctly classified and those incorrectly classified as tumor, respectively, versus a range of potential Cet-BPD fluorescence intensity thresholds. A dotted black line indicates the optimal threshold for tumor classification. (*C*) ROC analysis of Cet-BPD tumor selectivity. Minimum tumor size of 30 μm: 93% sensitivity and 93% specificity, ROC area under the curve (AUC) = 0.961, *n* = 12 mice (296 fields). (*D* and *E*) Maximum intensity projections of 3D confocal images (*D*) and quantitative analysis (*E*) demonstrate colocalization (mean ± SEM) of activated Cet-BPD with EOC cells but not with EC cells (anti-CD31 stain), *n* = 7 mice (262 optical sections; ****$P < 0.0001$, two-tailed unpaired *t* test). [Scale bars: 1 mm (*A*) and 100 μm (*D*).]

(ROC) analysis (Fig. 3*C*), attained 93% sensitivity and 93% specificity for micrometastases as small as 30 μm. Furthermore, high-magnification confocal depth scans of micrometastases revealed that 81% of Cet-BPD fluorescence colocalizes with EOC cells (Fig. 3 *D* and *E*, and Fig. S7).

To address the question of inflated tumor selectivity due to a lack of cross-reactivity with basal mouse EGFR levels, we investigated Cet-BPD binding to both mouse and human EGFR. The EGFR binding specificity, cellular internalization, and activation profiles of Cet-BPD(1:7) are similar for murine and human cells (Fig. S4). Furthermore, previous in vitro studies have shown that Cet-BPD is highly selective to cancer cells overexpressing EGFR surface molecules with 20-fold less accumulation in low EGFR-expressing cells (35). Hence, the tumor selectivity achieved by Cet-BPD is due to tumor-targeted activation.

Longitudinal Imaging of Immunoconjugate Pharmacokinetics. Characterization of immunoconjugate pharmacokinetics and tumor selectivity dynamics enables determination of optimal time points for micrometastasis imaging and for NIR irradiation to perform taPIT. We developed in vivo longitudinal imaging of immunoconjugate pharmacokinetics using fluorescence microendoscopy. In contrast to the biodistribution data presented above—where a separate group of mice was killed at each time point—this approach enables

longitudinal monitoring of individual mice, which significantly reduces both the use of animals and labor to characterize pharmacokinetics. To expedite interpretation of the acquired fluorescence microendoscopy images, we developed a rapid batch image processing workflow capable of automated and objective interpretation of the raw images. The workflow incorporates mean autofluorescence subtraction, pharmacokinetics-informed tumor thresholding, and correction factors for quantitative tumor burden imaging (Fig. S2) with >95% rejection of nonspecific fluorescence background for pixel-by-pixel tumor recognition (Fig. S3*A*). In vivo fluorescence microendoscopy indicated peak fluorescence intensity and tumor selectivity 8–24 h following Cet-BPD administration (Fig. 4*A*), in agreement with Cet-BPD tissue extraction (Pearson correlation *r* = 0.82, *n* = 21, $P = 5 \times 10^{-6}$; Fig. 4 *B* and *C*). To investigate the origins of tumor selectivity further, we performed fluorescence microendoscopy using two nonspecific, activatable immunoconjugate controls: (*i*) IgG-BPD(1:7) using polyclonal IgGs isolated from human serum; and (*ii*) Tra-BPD(1:5) using trastuzumab, a humanized anti-HER2 mAb. HER2 is a surface molecule from the EGFR family, but it is not expressed at the same level as EGFR by the EOC cells used in this study (Fig. 4 *E* and *F*). Both of the nonspecific immunoconjugate controls had altered pharmacokinetics (Fig. S8) and reduced tumor-to-tissue
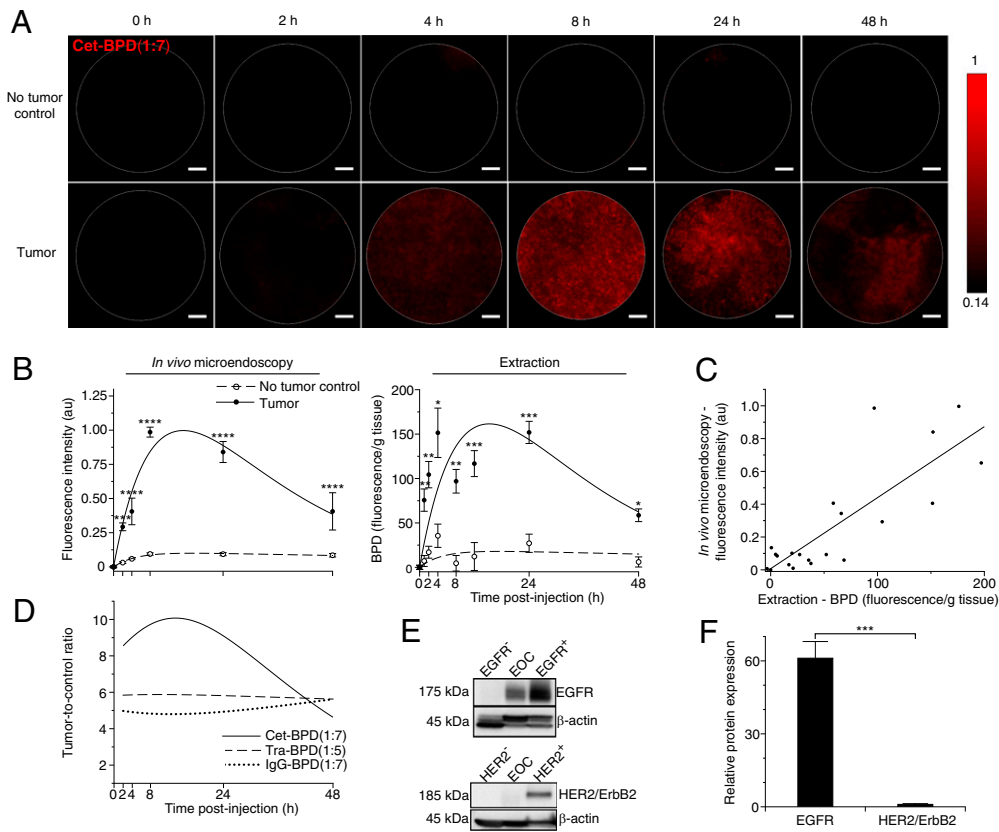
Spring et al.

Fig. 4. In vivo Cet-BPD tumor selectivity dynamics. (A) Longitudinal in vivo fluorescence microendoscopy shows Cet-BPD(1:7) micrometastasis specificity 8–24 h postadministration. (Scale bars: 100 μm.) (B) Mean ($\pm$ SEM) pharmacokinetic traces for Cet-BPD by fluorescence microendoscopy (40 fields per mouse) and extraction (including multiple tissue sites). The trend lines are fits to a simple pharmacokinetic model (*SI Text*). Fluorescence microendoscopy Cet-BPD: control, $n = 4$ mice; tumor, $n = 3$ mice. Extraction Cet-BPD (per time point): control, $n = 5$ mice; tumor, $n = 5$ mice (*$P < 0.05$, **$P < 0.01$, ***$P < 0.001$, ****$P < 0.0001$, two-tailed unpaired t test). (C) Tissue extraction studies validate Cet-BPD pharmacokinetic fluorescence microendoscopy. The plot includes the data in B and additional data for verteporfin (Fig. S8B). (D) Tumor selectivity dynamics by fluorescence microendoscopy for Cet-BPD, Tra-BPD (HER2-targeted mAb), and IgG-BPD (nonspecific, polyclonal antibody). Tra-BPD control, $n = 3$ mice; tumor, $n = 4$ mice. IgG-BPD control, $n = 4$ mice; tumor, $n = 3$ mice. (E) Western blot determination of relative EGFR and HER2 protein expression levels in EOC cells (positive and negative control cell lines are also shown). (F) Mean ($\pm$ SEM) EOC EGFR expression is higher than that of HER2 by blot densitometry, $n = 3$ replicates (***$P = 0.00016$, two-tailed unpaired t test).

ratios (Fig. 4D), underscoring the significance of selecting an appropriate target.

taPIT Selectively Destroys Micrometastases. There is a critical need for tumor-selective therapies that can address residual micrometastases. Above, we demonstrated that Cet-BPD(1:7) is activated selectively within tumors, resulting in enhanced tumor fluorescence contrast compared with always-on agents. We next tested whether this tumor-selective activation translates to a reduction in nonspecific phototoxicity. The fraction of EOC mice surviving taPIT, reflecting treatment safety and reduced toxicity in nontarget tissues, was enhanced for Cet-BPD(1:7) versus a nonoptimal immunoconjugate with lower quenching—Cet-BPD(1:4) (Fig. 5A). Furthermore, bowel histology confirmed that high-dose taPIT with Cet-BPD(1:7) does not cause bowel damage (Fig. S6A).

The light doses of 50–100 J·cm^{-1} per quadrant and the BPD dose of 2 mg·kg^{-1} enabled by taPIT exceed the maximum tolerated photodynamic dose—the maximum product of the light dose and the photodynamic agent dose at which 100% of EOC mice survive treatment—for nontargeted, always-on verteporfin [8 J·cm^{-1} per quadrant at a BPD dose of 0.25 mg·kg^{-1} (39)] by an order of magnitude (~50-fold). Furthermore, taPIT enables a ~17-fold increase in the maximum tolerated photodynamic dose compared with targeted, always-on immunoconjugates for PIT [0.5–1 mg·kg^{-1} photodynamic agent with 3–6 J·cm^{-1} per quadrant (21, 23, 40)]. Thus, taPIT enables unprecedented photodynamic doses for

treating disseminated metastatic disease by overcoming nonspecific toxicities associated with—both targeted and nontargeted—always-on agents.

To explore the potency of high-dose taPIT against microscopic tumors in large cavities, EOC mice bearing disseminated micrometastases were treated using a diffusing tip fiber for wide-field irradiation (Fig. 1F). A quantitative reverse transcription–PCR (qRT-PCR) assay was used to assess the number of viable, human EOC cells rigorously in biopsies and entire peritoneal cavities following treatment (*SI Text* and Fig. S9 A and B). Control, untreated EOC mice were characterized for the final tumor burden by qRT-PCR at time points matched to the various treatment courses (Fig. S9 C–E). Treated mice received i.p. administration of the immunoconjugate in the presence or absence of photoactivation. We observed a trend in reduced number of EOC cells using Cet-BPD(1:7) in the absence of photoactivation (Fig. 5B), which indicates that Cet-BPD possesses similar anti-EGFR and antitumor activity to cetuximab monotherapy (12, 36). NIR photoactivation for taPIT (two cycles) achieved a statistically significant mean reduction in tumor burden of 89% relative to untreated mice (Fig. 5B). This level of tumor reduction matches the synergistic reduction found using unconjugated BPD (two cycles) and cetuximab (four cycles) in combination (12). As a benchmark for nearly complete response, taPIT (one cycle) with follow-up combination platinum- and taxane-based chemotherapy (one cycle) achieves 97% mean tumor burden reduction
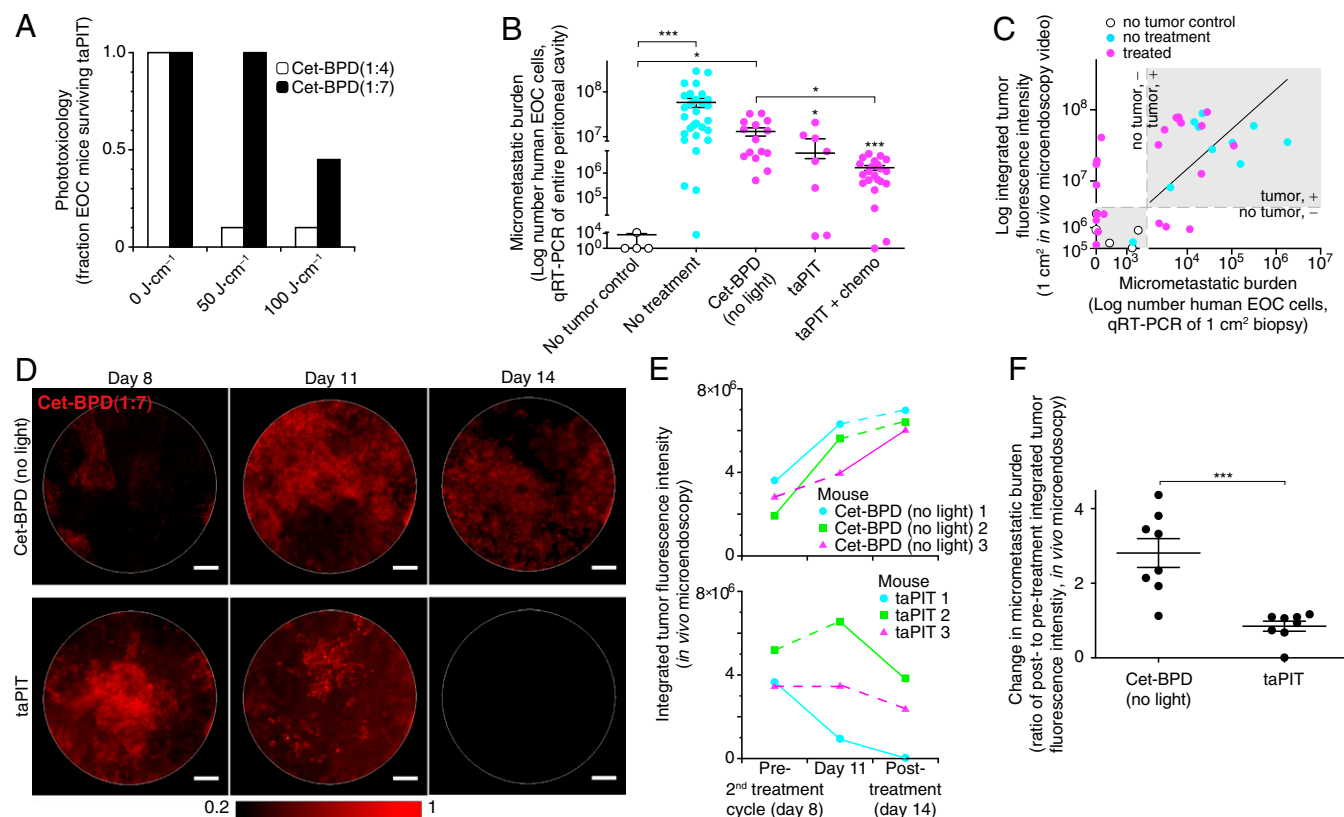
Fig. 5. taPIT toxicology, efficacy, and longitudinal monitoring of micrometastatic burden in vivo. (*A*) Fraction of tumor-bearing mice that survived >72 h after taPIT. Cet-BPD(1:7) shows increased survival and reduced nonspecific phototoxicity compared with Cet-BPD(1:4). Cet-BPD(1:4): 0 (*n* = 9 mice), 50 (*n* = 10 mice), and 100 J·cm^{-1} (*n* = 10 mice). Cet-BPD(1:7): 0 (*n* = 16 mice), 50 (*n* = 19 mice), and 100 J·cm^{-1} (*n* = 20 mice). (*B*) Micrometastatic burden measured by qRT-PCR: no-tumor control, *n* = 4 mice; no treatment, *n* = 30 mice; Cet-BPD (no light, one to two treatment cycles), *n* = 15 mice; taPIT (50 J·cm^{-1}, two cycles), *n* = 8 mice; taPIT and chemotherapy (50–100 J·cm^{-1}, one to two cycles), *n* = 22 mice. The asterisks denote statistically significant differences compared with un-treated EOC mice, or among the indicated treatment groups (*P < 0.05, ***P < 0.001, Kruskal–Wallis one-way ANOVA test). (*C*) The integrated tumor signal from in vivo fluorescence microendoscopy movies of 1-cm^2 biopsies (Movies S1–S4) compared with qRT-PCR analysis performed on matched specimens. The shaded regions indicate biopsies found to either be tumor negative (lower left box) or positive (upper right box) by both in vivo imaging and qRT-PCR. (*D*) Longitudinal fluorescence microendoscopy during Cet-BPD (no light) and taPIT treatment regimens. (Scale bars: 100 μm.) (*E*) Quantification of exemplary, individual mouse tumor fluorescence signals during the treatment time course. The solid lines indicate significant changes (P < 0.05, two-tailed unpaired *t* test). (*F*) Fluorescence microendoscopy-based normalization of the post- by the pretreatment tumor burden corrects interpatient variability to reveal en-hanced taPIT efficacy over Cet-BPD without photoactivation. In *B* and *F*, the mean ± SEM is overlaid on the scatter plots of individual results: Cet-BPD (no light, two cycles), *n* = 8 mice; taPIT (50 J·cm^{-1}, two cycles), *n* = 8 mice (***P < 0.001, Mann–Whitney *U* test).

(Fig. 5*A*; a second cycle added no significant benefit). As a fur-ther comparative benchmark, prior work indicates 10% and 50% tumor burden reduction for one and two cycles, respectively, of combination cisplatin plus paclitaxel chemotherapy—at the same doses used here (*Materials and Methods*)—in this mouse model of metastatic ovarian cancer (23). The relatively poor response to chemotherapy alone may be due to intrinsic resistance—the OVCAR5 cells used in this model have sevenfold resistance to cisplatin relative to a platinum-sensitive cell line (31) and contain a subpopulation of stem-like cells that are stimulated by che-motherapy (8).

Longitudinal Micrometastatic Burden Monitoring. A key challenge associated with micrometastatic disease is the lack of imaging modalities capable of resolving and monitoring microscopic tumors. Building on the selective accumulation of activated Cet-BPD in micrometastases, which enables accurate recognition of microscopic tumors in untreated mice, we developed micro-metastatic burden monitoring using longitudinal fluorescence microendoscopy. The image analysis workflow described above was used as a surrogate marker for micrometastatic burden (Fig. S2). This surrogate was compared with the qRT-PCR assay in matched biopsy specimens from individual untreated and treated

EOC mice. Validation of fluorescence microendoscopy tumor monitoring by qRT-PCR indicates a significant Spearman cor-relation $r = 0.59$ ($P = 0.0001$) and a tumor recognition sensitivity of 86% and specificity of 73% ($n = 37$ mice) (Fig. 5*C*). The gray regions in Fig. 5*C* define the true negatives (*Lower Left*; using control no-tumor mice to define the bounds) and true positives (*Upper Right*). The false-positive and -negative outliers are treated mice. False positives are due to residual, tumor-associated in-flammation (*SI Text*, Note S6, and Fig. S10). False negatives are likely due to insufficient sampling of the residual disease after treatment. Exclusion of treated mice results in a Spearman cor-relation $r = 0.70$ ($P = 0.004$) and a tumor recognition sensitivity of 100% and specificity of 100% ($n = 15$ mice).

Longitudinal fluorescence microendoscopy imaging of tumor burden in mice receiving taPIT versus Cet-BPD (without pho-toactivation) is shown over time (Fig. 5 *D* and *E*). In each mouse receiving taPIT, the integrated tumor fluorescence decreased markedly between days 11 and 14. Note that taPIT was also performed on day 5; thus, some of these mice display reductions in tumor burden before day 8. Using the same metric, mice ex-posed to Cet-BPD (without photoactivation) showed evidence of increasing tumor burden (Fig. 5*D*). These data demonstrate that, when the pretreatment tumor burden is taken into account, the
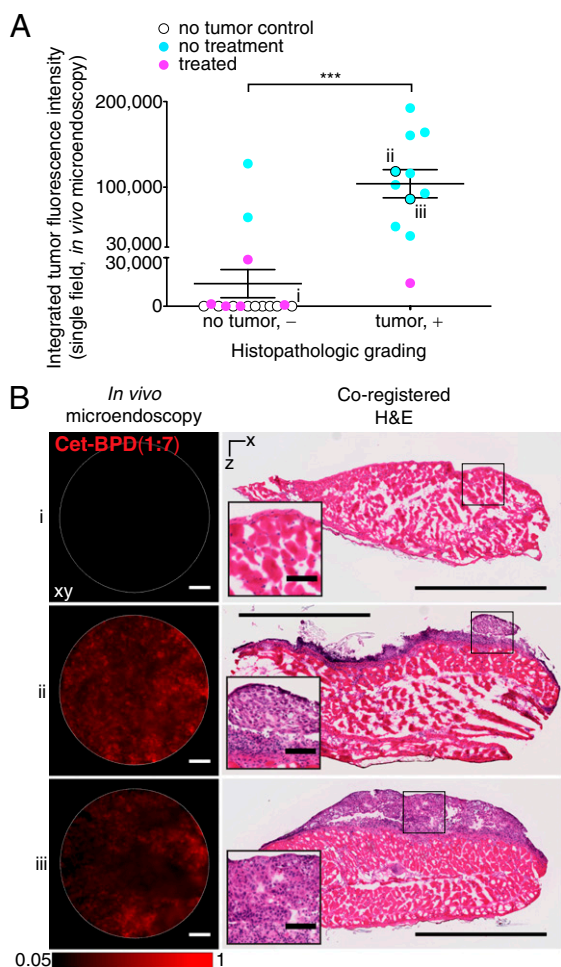
Fig. 6. Histopathologic validation of micrometastasis recognition by in vivo fluorescence microendoscopy. (*A*) Comparison of tumor signal by in vivo fluorescence microendoscopy to histopathologic grading of coregistered punch biopsies. The mean ± SEM is overlaid on scatter plots: no tumor, *n* = 16 mice; tumor, *n* = 11 mice (***$P < 0.001$, Mann–Whitney *U* test). (*B*) Exemplary coregistered *en face* fluorescence microendoscopy images and vertically sectioned, H&E-stained biopsies for the data points labeled *i–iii* in *A*. [Scale bars: 100 μm (for fluorescence microendoscopy and H&E *Insets*) and 1 mm (for H&E image mosaics).]

enhanced therapeutic efficacy of taPIT over Cet-BPD (without photoactivation) is clearly resolved (Fig. 5*F*). Without this correction, treatment efficacy is more difficult to discern due to the intrinsic heterogeneity of microscopic disease. Thus, quantitative micrometastatic burden imaging will be critical for evaluation of treatment efficacy in preclinical and clinical studies of residual microscopic disease.

To probe tumor recognition accuracy further, we collected punch biopsies for histopathology coregistered with in vivo fluorescence microendoscopy images. A blinded pathologist graded the hematoxylin and eosin (H&E)-stained sections as either "no tumor, −" in the absence of clear tumor nodules or "tumor, +" in the presence of multicellular tumor nodules. The resulting histopathologic grades are compared with integrated, in vivo tumor fluorescence (Fig. 6*B*). The integrated tumor fluorescence was significantly lower for "no tumor, −" than for "tumor, +" biopsies (Fig. 6*A*). In fields where Cet-BPD fluorescence could not be detected, no tumor was observed by histopathology. These data provide a further validation of in vivo fluorescence microendoscopy, indicating a tumor recognition sensitivity of 91% and specificity of 88% (*n* = 13 mice) (27 fields). Finally, histopathologic review of these punch biopsies

provides further evidence of tumor destruction by taPIT and taPIT with follow-up chemotherapy (Fig. S6 *B* and *C*).

Discussion

taPIT is a therapeutic modality that achieves selective treatment of residual and micrometastatic cancer. Uniquely, Cet-BPD incorporates two synergistic therapies into a single agent— with the photocytotoxic component remaining quenched in nonspecific tissues—to realize a molecular-targeted, activatable therapy. Because cancer cells overexpressing the target surface molecules take up immunoconjugates efficiently (28, 35, 37) (Fig. S4), this activation occurs predominantly within tumors while unbound conjugates remain quenched. Enhanced lysosomal catabolism of immunoconjugates—which ultimately activates photocytotoxicity and fluorescence—is also expected in cancer cells due to their frequent, high up-regulation of cysteine cathepsin proteases (41). This tumor-targeted activation (terminology clarified in *SI Text*, Note S7) enhances contrast for imaging and selective therapy of micrometastases, minimizing background fluorescence and toxicity to vital tissues.

Prior elegant works have demonstrated selective tumor imaging using activatable contrast agents, primarily of macroscopic tumors (17, 28, 29, 42–44). However, these probes have not been used to treat micrometastases, largely due to the fact that fluorescence-guided surgery is impractical at the microscopic scale. In addition, quantitative imaging of microscopic tumor deposits has yet to be investigated using always-on or activatable probes. Here, we show—importantly, in a disease model that presents challenges to selectivity encountered in the clinic—that directly targeting the cancer cells for immunoconjugate activation enables not only enhanced treatment selectivity but also resolution of individual micrometastases.

PIT is an emerging treatment modality that bolsters the armamentarium of cancer treatments. Photodynamic therapy and PIT induce cytotoxicity using mechanisms that are distinct from traditional therapies (12–14) to overcome resistance (19, 20, 23) and stimulate, rather than suppress, antitumor immunity (14). For example, photodynamic action can trigger apoptosis through direct photodamage of Bcl-2 protein (13), which is a major cause of radioresistance and chemoresistance (45). With the frequent use of fiber optics in medical procedures, light delivery can be and has been successful clinically in complex anatomical sites such as the peritoneal cavity and the lung. Therefore, in the clinic, these agents are photoactivated intraoperatively or endoscopically. Early clinical trials demonstrated feasibility and efficacy for photodynamic therapy of peritoneal metastases (27) with the major challenge being bowel perforations resulting from a lack of tumor selectivity (38). taPIT overcomes this poor tumor selectivity and bowel toxicity. In contrast to conventional PIT and photodynamic therapy, the enhanced therapeutic index of taPIT addresses challenges associated with the delivery of treatment to microscopic disease spread throughout large sites such as the peritoneal cavity.

Microendoscopy has taken microscopy to new depths in vivo using miniaturized optics (46), and this technology is emerging for "optical biopsy" of cancer (32, 47–53). Through the development of in vivo fluorescence microendoscopy with activatable immunoconjugates and automated image analysis algorithms (Fig. S2), we demonstrated that it is possible to monitor micrometastases longitudinally. The sensitivity and specificity of ∼90% achieved here for untreated tumors as small as 30 μm represents a significant improvement over the 86% and 53% tumor sensitivity and specificity reported for always-on verteporfin (32). This level of selectivity also results in a two order-of-magnitude improvement in tumor-imaging resolution compared with current clinical imaging technologies (e.g., positron emission tomography, computed tomography, and magnetic resonance imaging), which have 40–50% sensitivity for subcentimeter tumors (10, 11). These developments address the lack of imaging technologies for

detecting and monitoring micrometastatic disease (3) and open the door to patient-tailored therapeutic regimens based upon real-time feedback regarding the presence and response of residual disease. Here, we also developed fluorescence microendoscopy for pharmacokinetic imaging to shape dosimetry decisions and to inform tumor recognition algorithms (Fig. 4 and Fig. S2). The miniature size and mechanical flexibility of fiber-optic fluorescence microendoscopy enable minimally invasive and repeated quantification of micrometastases.

Presently, it is only practical to sample some—but not all—of the total micrometastatic burden by microendoscopy due to the microscopic field of view, whereas taPIT can be applied for wide-field treatment of large regions of the body harboring disseminated tumors efficiently without the need to first visualize each micrometastasis (SI Text, Note S8). Future microendoscope designs may use larger fiber bundles—or foveated lens systems (54)—to expand the field of view and to enable scanning comparable to conventional laparoscopy.

In the clinic, a number of obstacles have hampered attempts to address cancer micrometastases despite their critical role in treatment failure. Two major barriers are the inability to detect residual tumor deposits until macroscopic recurrence and poor patient tolerance of the chemotherapy dose intensities needed for tumor response (55) coupled with the emergence of chemoresistance (2, 8). The enhanced tumor selectivity realized by tumor-targeted, activatable immunoconjugates, along with evidence that PIT is effective against drug-resistant cells, offers promise to help overcome these hurdles. taPIT holds potential to improve cancer survival by leveraging the distinct mechanisms of photodynamic action (13) to treat drug-resistant cells (26) and reverse chemoresistance (20), thereby reducing the number of cycles of chemotherapy needed to elicit tumor destruction (23). In addition, rationally designed immunoconjugates simultaneously inhibit treatment survival signaling pathways [e.g., the EGFR pathway (56)] in concert with their photocytotoxic effects (36). Molecular tumor targeting also provides opportunities for fluorescence-guided surgery (15–17) to remove more disease before taPIT and chemotherapy.

Thus, activatable immunoconjugates show promise for clinical translation to address recurrent cancers by facilitating fluorescence-guided resection of macroscopic tumors and fluorescence microendoscopy-guided taPIT to destroy, monitor, and potentiate follow-up chemotherapy of residual microscopic disease. In regard to therapy monitoring, the same phenomenon of tumor-targeted activation for PIT also enables detection of residual microscopic disease in critical areas using fluorescence microendoscopy, which may ultimately facilitate the clinical diagnosis of recurrent disease at earlier time points than possible using traditional technologies.

Materials and Methods

Micrometastatic Mouse Model. An orthotopic xenograft mouse model of human ovarian carcinomatosis was established in our laboratory with gynecologic oncologists (30). Athymic Swiss female Nu/Nu mice (20–25 g and 6–8 wk old; Cox Breeding Laboratories) were injected i.p. with 16×10^6 NIH:OVCAR5 (EOC) cells in 2 mL of PBS. All experiments were conducted according to Massachusetts General Hospital Institutional Animal Care and Use Committee guidelines.

Immunoconjugate Synthesis. Conjugates of BPD and mAb (Cet or Tra) or human polyclonal antibody (IgG; I4506; Sigma-Aldrich) were prepared by modifying a previous protocol (35) for large-scale synthesis and administered at 2 mg·kg⁻¹ body weight BPD, except in Fig. 2B for which an equivalent mAb dose was used (1.4 mg of cetuximab) to ensure identical mAb pharmacokinetics for quantitative assessment of nonspecific fluorescence. Briefly, the N-hydroxysuccinimide ester of BPD was reacted with antibody, which had previously been polyethylene glycolated. The resulting immunoconjugate was purified using a Zeba spin desalting column (Thermo Scientific). The purity of the immunoconjugates is high—as assessed by gel fluorescence imaging analysis following SDS polyacrylamide gel electrophoresis—with less than 5% residual unconjugated BPD impurity (an upper

bound because fluorescence quenching of conjugated BPD was not taken into account) (35). The molar ratio of BPD to antibody was measured using a BCA Protein Assay (Pierce) and BPD absorbance spectroscopy at 690 nm.

Intraperitoneal taPIT and Chemotherapy. EOC mice were randomized into the following groups: (i) no treatment; (ii) Cet-BPD without taPIT (0 J·cm⁻¹), one cycle; (iii) Cet-BPD without taPIT (0 J·cm⁻¹), two cycles; (iv) Cet-BPD with taPIT (50 J·cm⁻¹), two cycles; and (v) Cet-BPD with taPIT (50–100 J·cm⁻¹), combined with 3–5 and 10–15 mg·kg⁻¹ body weight of cisplatin and paclitaxel, one to two cycles (Fig. S9 C–E). All injections were done i.p. in 1 mL of sterile PBS. The BPD dose was fixed at 2 mg·kg⁻¹ body weight. For Cet-BPD (1:7), the cetuximab dose was 1.4 mg, which is equivalent to ~180 mg·m⁻² and near the clinical cetuximab dose of 250–400 mg·m⁻². Treatment-associated mortality is defined as mice surviving less than 72 h after treatment. Timelines for the various treatment regimens are shown in Fig. S9 C–E. Mice were illuminated 8–24 h (taPIT) after immunoconjugate injection as follows. Mice were anesthetized with isoflurane during treatment and imaging. The light doses are defined as the energy delivered per unit length of the diffusing fiber tip per peritoneal quadrant (i.e., one-fourth of the total fluence per mouse). We performed i.p. light irradiation as previously described (12). Briefly, all mice were injected i.p. with 2 mL of a 0.1% intralipid solution (Baxter Healthcare) to enhance light scattering. A cylindrically diffusing-tip fiber, connected to a 690-nm diode laser (High Power Devices), was introduced into the peritoneal cavity of a supine anesthetized animal via a centrally placed 14-gauge catheter that traversed the peritoneal wall. The 690-nm light was delivered at an irradiance of 150 (for 50 J·cm⁻¹ taPIT) or 300 mW·cm⁻¹ (for 100 J·cm⁻¹ taPIT). One-fourth of the total light energy was delivered to each i.p. quadrant over equivalent periods.

In Vivo Fluorescence Microendoscopy. During fluorescence microendoscopy of anesthetized mice (using isoflurane inhalant anesthesia), we acquired 40 snapshots per mouse per time point during 10 frames per second (fps) movie preview. The snapshots were distributed evenly among the peritoneal wall and pelvic omentum. For fluorescence microendoscopy validation, we marked a 1-cm² region on the outer peritoneal wall using a tissue marking dye (Mark-It; Richard-Allan Scientific), after peeling back the neighboring skin. We then collected a 10-fps in vivo fluorescence microendoscopy movie of Cet-BPD(1:7) fluorescence by scanning over the inner peritoneal wall within the marked region. Exemplary movies are provided (Movies S1–S4)—all of the movies are displayed on the same intensity scale (the same scale shown in Fig. 4A) and show 100 of 600 total frames. To perform fluorescence microendoscopy-guided biopsy, we then placed the microendoscope tip at a field of interest and marked the location with a dot of marking dye on the outer wall. The square piece of tissue was then excised and we collected the marked location using a punch biopsy (3-mm diameter; Miltex), followed by immediate embedding and freezing of the biopsy in optimal cutting temperature compound for frozen sectioning on a microtome–cryostat. We avoided directly handling tissue biopsies by dispensing them onto lens paper followed by application of embedding medium. The tissue paper was then held vertically in cryomolds using forceps to orient the punch biopsies for vertical sectioning, perpendicular to the peritoneal wall surface. This procedure enables coregistered microendoscope images and biopsy specimens for histopathology and immunofluorescence staining. The square piece of tissue was then snap frozen for qRT-PCR to compare with tumor burden assessment by fluorescence microendoscopy. Verteporfin and Cet-BPD were administered at equivalent BPD doses (2 mg·kg⁻¹ body weight), except for (Fig. 2B) as noted above.

Fluorescence Microendoscopy Image Analysis. For the control no-tumor mice, we calculated the mean fluorescence signal intensity and calculated an intensity threshold set to classify 99.5% of the pixels as "no tumor" (Fig. S3). For the EOC mice, we calculated the mean fluorescence signal intensity for pixels above the no-tumor threshold, and only for objects greater than 30 μm in dimension based on the ROC analysis (Fig. 3). The reported values for EOC mice were calculated from the five brightest images per mouse. In all cases, the mean autofluorescence intensity (determined by imaging mice before immunoconjugate injection) was subtracted, and an automated routine was used to select the fiber bundle in each image for analysis (indicated by a white circle in the figures). All analyses were performed using a custom Matlab routine for batch image processing (Fig. S2).

Statistical Analysis. Statistical analyses were carried out using GraphPad Prism (GraphPad Software). Specific statistical tests are indicated in the figure captions. Tumor burden reduction data among multiple treatment groups were analyzed using a Kruskal–Wallis one-way ANOVA following a Grubbs' test that identified statistical outliers. No more than one outlier

was removed per treatment group. Two-tailed *P* values are reported for Pearson and Spearman correlation coefficients. The Spearman correlation coefficients (representing nonlinear, monotonic correlations) were used for micrometastatic burden imaging validations because integrated tumor fluorescence scales as a power law with tumor volume (32).

Additional details on experimental procedures and data processing used for this study can be found in *SI Text*, *Fluorescence Microendoscope*, *In Vitro Validations of Cet-BPD Specificity and Immunofluorescence Stains*, *Hyperspectral Imaging of the Peritoneal Cavity*, *BPD Quantifica-tion by Tissue Extraction*, *Pharmacokinetic Model*, *Confocal Imaging of Freshly Excised Tissues*, *Western Blots*, and *Quantitative RT-PCR Measurement of Micrometastatic Burden.*

1. Naora H, Montell DJ (2005) Ovarian cancer metastasis: Integrating insights from disparate model organisms. *Nat Rev Cancer* 5(5):355–366.
2. Bast RC, Jr., Hennessy B, Mills GB (2009) The biology of ovarian cancer: New opportunities for translation. *Nat Rev Cancer* 9(6):415–428.
3. Pantel K, Alix-Panabières C, Riethdorf S (2009) Cancer micrometastases. *Nat Rev Clin Oncol* 6(6):339–351.
4. Lengyel E (2010) Ovarian cancer development and metastasis. *Am J Pathol* 177(3):1053–1064.
5. Nguyen DX, Bos PD, Massagué J (2009) Metastasis: From dissemination to organ-specific colonization. *Nat Rev Cancer* 9(4):274–284.
6. Glehen O, et al. (2004) Cytoreductive surgery combined with perioperative intraperitoneal chemotherapy for the management of peritoneal carcinomatosis from colorectal cancer: A multi-institutional study. *J Clin Oncol* 22(16):3284–3292.
7. Hidalgo M (2010) Pancreatic cancer. *N Engl J Med* 362(17):1605–1617.
8. Meirelles K, et al. (2012) Human ovarian cancer stem/progenitor cells are stimulated by doxorubicin but inhibited by Mullerian inhibiting substance. *Proc Natl Acad Sci USA* 109(7):2358–2363.
9. Selman AE, Copeland LJ (1999) The roles of second-look laparotomy and cancer antigen 125 in the management of ovarian carcinoma. *Curr Oncol Rep* 1(1):71–76.
10. Gadducci A, et al. (2007) Surveillance procedures for patients treated for epithelial ovarian cancer: A review of the literature. *Int J Gynecol Cancer* 17(1):21–31.
11. Soussan M, et al. (2012) Comparison of FDG-PET/CT and MR with diffusion-weighted imaging for assessing peritoneal carcinomatosis from gastrointestinal malignancy. *Eur Radiol* 22(7):1479–1487.
12. del Carmen MG, et al. (2005) Synergism of epidermal growth factor receptor-targeted immunotherapy with photodynamic treatment of ovarian cancer in vivo. *J Natl Cancer Inst* 97(20):1516–1524.
13. Kessel D (2006) Death pathways associated with photodynamic therapy. *Med Laser Appl* 21(4):219–224.
14. Castano AP, Mroz P, Hamblin MR (2006) Photodynamic therapy and anti-tumour immunity. *Nat Rev Cancer* 6(7):535–545.
15. van Dam GM, et al. (2011) Intraoperative tumor-specific fluorescence imaging in ovarian cancer by folate receptor-α targeting: First in-human results. *Nat Med* 17(10):1315–1319.
16. Stummer W, et al. (2006) Fluorescence-guided surgery with 5-aminolevulinic acid for resection of malignant glioma: A randomised controlled multicentre phase III trial. *Lancet Oncol* 7(5):392–401.
17. Nguyen QT, et al. (2010) Surgery with molecular fluorescence imaging using activatable cell-penetrating peptides decreases residual cancer and improves survival. *Proc Natl Acad Sci USA* 107(9):4317–4322.
18. Mew D, Wat CK, Towers GH, Levy JG (1983) Photoimmunotherapy: Treatment of animal tumors with tumor-specific monoclonal antibody-hematoporphyrin conjugates. *J Immunol* 130(3):1473–1477.
19. Goff BA, Bamberg M, Hasan T (1991) Photoimmunotherapy of human ovarian carcinoma cells ex vivo. *Cancer Res* 51(18):4762–4767.
20. Duska LR, Hamblin MR, Miller JL, Hasan T (1999) Combination photoimmunotherapy and cisplatin: Effects on human ovarian cancer ex vivo. *J Natl Cancer Inst* 91(18):1557–1563.
21. Molpus KL, Hamblin MR, Rizvi I, Hasan T (2000) Intraperitoneal photoimmunotherapy of ovarian carcinoma xenografts in nude mice using charged photoimmunoconjugates. *Gynecol Oncol* 76(3):397–404.
22. Soukos NS, et al. (2001) Epidermal growth factor receptor-targeted immunophotodiagnosis and photoimmunotherapy of oral precancer in vivo. *Cancer Res* 61(11):4490–4496.
23. Rizvi I, et al. (2012) Photoimmunotherapy and irradiance modulation reduce chemotherapy cycles and toxicity in a murine model for ovarian carcinomatosis: Perspective and results. *Isr J Chem* 52(8-9):776–787.
24. van Dongen GA, Visser GW, Vrouenraets MB (2004) Photosensitizer-antibody conjugates for detection and therapy of cancer. *Adv Drug Deliv Rev* 56(1):31–52.
25. Mitsunaga M, et al. (2011) Cancer cell-selective in vivo near infrared photoimmunotherapy targeting specific membrane molecules. *Nat Med* 17(12):1685–1691.
26. Celli JP, Solban N, Liang A, Pereira SP, Hasan T (2011) Verteporfin-based photodynamic therapy overcomes gemcitabine insensitivity in a panel of pancreatic cancer cell lines. *Lasers Surg Med* 43(7):565–574.
27. Hahn SM, et al. (2006) A phase II trial of intraperitoneal photodynamic therapy for patients with peritoneal carcinomatosis and sarcomatosis. *Clin Cancer Res* 12(8):2517–2525.
28. Urano Y, et al. (2009) Selective molecular imaging of viable cancer cells with pH-activatable fluorescence probes. *Nat Med* 15(1):104–109.
29. Lee H, et al. (2011) Near-infrared pH-activatable fluorescent probes for imaging primary and metastatic breast tumors. *Bioconjug Chem* 22(4):777–784.
30. Molpus KL, et al. (1996) Characterization of a xenograft model of human ovarian carcinoma which produces intraperitoneal carcinomatosis and metastases in mice. *Int J Cancer* 68(5):588–595.
31. Roberts D, et al. (2005) Identification of genes associated with platinum drug sensitivity and resistance in human ovarian cancer cells. *Br J Cancer* 92(6):1149–1158.
32. Zhong W, et al. (2009) In vivo high-resolution fluorescence microendoscopy for ovarian cancer detection and treatment monitoring. *Br J Cancer* 101(12):2015–2022.
33. Psyrri A, et al. (2005) Effect of epidermal growth factor receptor expression level on survival in patients with epithelial ovarian cancer. *Clin Cancer Res* 11(24 Pt 1):8637–8643.
34. Mendelsohn J, Baselga J (2003) Status of epidermal growth factor receptor antagonists in the biology and treatment of cancer. *J Clin Oncol* 21(14):2787–2799.
35. Savellano MD, Hasan T (2003) Targeting cells that overexpress the epidermal growth factor receptor with polyethylene glycolated BPD verteporfin photosensitizer immunoconjugates. *Photochem Photobiol* 77(4):431–439.
36. Abu-Yousif AO, et al. (2012) Epidermal growth factor receptor-targeted photosensitizer selectively inhibits EGFR signaling and induces targeted phototoxicity in ovarian cancer cells. *Cancer Lett* 321(2):120–127.
37. Savellano MD, Hasan T (2005) Photochemical targeting of epidermal growth factor receptor: A mechanistic study. *Clin Cancer Res* 11(4):1658–1668.
38. Cengel KA, Glatstein E, Hahn SM (2007) Intraperitoneal photodynamic therapy. *Cancer Treat Res* 134:493–514.
39. Molpus KL, et al. (1996) Intraperitoneal photodynamic therapy of human epithelial ovarian carcinomatosis in a xenograft murine model. *Cancer Res* 56(5):1075–1082.
40. Goff BA, Blake J, Bamberg MP, Hasan T (1996) Treatment of ovarian cancer with photodynamic therapy and immunoconjugates in a murine ovarian cancer model. *Br J Cancer* 74(8):1194–1198.
41. Mohamed MM, Sloane BF (2006) Cysteine cathepsins: Multifunctional enzymes in cancer. *Nat Rev Cancer* 6(10):764–775.
42. Weissleder R, Tung CH, Mahmood U, Bogdanov A, Jr. (1999) In vivo imaging of tumors with protease-activated near-infrared fluorescent probes. *Nat Biotechnol* 17(4):375–378.
43. Liu TW, et al. (2011) Imaging of specific activation of photodynamic molecular beacons in breast cancer vertebral metastases. *Bioconjug Chem* 22(6):1021–1030.
44. Lovell JF, et al. (2011) Porphysome nanovesicles generated by porphyrin bilayers for use as multimodal biophotonic contrast agents. *Nat Mater* 10(4):324–332.
45. Reed JC, et al. (1996) BCL-2 family proteins: Regulators of cell death involved in the pathogenesis of cancer and resistance to therapy. *J Cell Biochem* 60(1):23–32.
46. Flusberg BA, et al. (2005) Fiber-optic fluorescence imaging. *Nat Methods* 2(12):941–950.
47. Lüdicke F, et al. (2003) Photodynamic diagnosis of ovarian cancer using hexaminolaevulinate: A preclinical study. *Br J Cancer* 88(11):1780–1784.
48. Yelin D, et al. (2006) Three-dimensional miniature endoscopy. *Nature* 443(7113):765.
49. Hsiung P-L, et al. (2008) Detection of colonic dysplasia in vivo using a targeted heptapeptide and confocal microendoscopy. *Nat Med* 14(4):454–458, correction (2008) 14(5):585.
50. Kim P, et al. (2010) In vivo wide-area cellular imaging by side-view endomicroscopy. *Nat Methods* 7(4):303–305.
51. John R, et al. (2010) In vivo magnetomotive optical molecular imaging using targeted magnetic nanoprobes. *Proc Natl Acad Sci USA* 107(18):8085–8090.
52. Williams RM, et al. (2010) Strategies for high-resolution imaging of epithelial ovarian cancer by laparoscopic nonlinear microscopy. *Transl Oncol* 3(3):181–194.
53. Pierce MC, et al. (2012) A pilot study of low-cost, high-resolution microendoscopy as a tool for identifying women with cervical precancer. *Cancer Prev Res (Phila)* 5(11):1273–1279.
54. Hagen N, Tkaczyk TS (2012) Foveated endoscopic lens. *J Biomed Opt* 17(2):021104.
55. Fauci JM, et al. (2011) Prognostic significance of the relative dose intensity of chemotherapy in primary treatment of epithelial ovarian cancer. *Gynecol Oncol* 122(3):532–535.
56. Mendelsohn J, Baselga J (2000) The EGF receptor family as targets for cancer therapy. *Oncogene* 19(56):6550–6565.

www.manaraa.com